Desalination and Water Treatment
www.deswater.com
doi: 10.1080/19443994.2015.1012561

57 (2016) 6723–6731
March

Taylor & Francis
Taylor & Francis Group

Investigating on photocatalytic performance of CuO micro and nanostructures prepared by different precursors

S. Safa[a], R. Azimirad[b], S. Safalou Moghaddam[c], M. Rabbani[c,*]

[a]*Young Researchers and Elite Club, South Tehran Branch, Islamic Azad University, Tehran, Iran, Tel./Fax: +98 2122974546; email: sda.safa@gmail.com*
[b]*Institute of Physics, Malek-Ashtar University of Technology, Tehran, Iran, Tel./Fax: +98 2122974546; email: azimirad@yahoo.com*
[c]*Department of Chemistry, Iran University of Science and Technology, Tehran 16846 13114, Iran, Tel. +98 21 77240290; Fax: +98 21 77491204; emails: sam.safalo@gmail.com (S. Safalou Moghaddam), m_rabani@iust.ac.ir (M.Rabbani)*

Received 2 July 2014; Accepted 22 January 2015

ABSTRACT

In this paper, various morphologies of copper oxide (CuO) were synthesized from acetate, sulfate, and nitrate precursors using hydrothermal bath method. The photoluminescence spectra revealed that CuO-Ni sample contains the strongest surface defect peak which can be related to its highest active surface area. The Fourier transform infrared (FT-IR) results showed that the concentration of the surface OH^- group on the samples varies considerably according to CuO-Ac > CuO-Ni > CuO-Su. From structural results, it could be observed that all the samples crystallized into a monoclinic crystal structure. The photocatalytic activity of CuO samples was evaluated by the catalytic oxidation of methylene blue in the presence of hydrogen peroxide. Concerning the nearly same optical band gap for the samples, the best photocatalytic performance of CuO-Ni nanorods was assigned to its highest active surface area and surface hydroxyl groups.

Keywords: Copper oxide; Micro- and nano-hierarchical; Photocatalyst; Methylene blue

1. Introduction

In the recent years, copper oxide (CuO) nanostructures have attracted great interest among researchers because of their interesting properties [1]. CuO, as a versatile p-type transition metal oxide semiconductor with a narrow band gap (ranging from 1.2 to 1.6 eV), has been extensively investigated in various fields such as gas sensors [2], solar energy transformation systems [3,4], heterogeneous catalysis [5], lithium-ion electrodes [6], magnetic materials [7], and superconductors [8]. Beside these applications, CuO has been proposed as an effective photocatalyst under visible and ultraviolet (UV) light irradiation [9–12]. Therefore, it could be concluded that fabrication of well-defined CuO nanostructures optimizes their performance in photocatalytic applications [13]. In this regard, various morphologies of CuO such as nanoparticles [14,15], nanoribbons [16,17], networks [18], nanoneedles [19], nanoshuttles [20], nanoflowers [21], nano-hierarchicals [22,23], and hollow microspheres [9] have been synthesized and studied in different applications.

Concerning the photocatalytic applications, Zaman et al. [24] observed that the size and morphology of

*Corresponding author.

CuO nanostructures are two important parameters affecting their performance against methylene blue (MB) and rhodamine B (RB). In fact, they found that the CuO petals show higher visible photocatalytic activity than the flower-like morphology. Shi et al. [25] synthesized CuO nanorods using a microwave method and observed that CuO nanorods with higher surface area have a relatively faster degradation rate against RB compared with other morphologies of CuO. Nevertheless, one can see a gap of study on the effects of CuO morphologies, surface functional groups, and surface defects on the photodegradation of a common dye pollutant which is the main object of this work. The strategy for producing various morphologies is on the base of changing CuO precursors which can form interesting shapes and morphologies in the presence of a surfactant. In this work, three different morphologies of CuO nanostructures were prepared using the various precursors in the presence of cetyltrimethylammonium bromide (CTAB) and urea as a surfactant and a hydrolysis agent, respectively. The prepared CuO nanostructures were photocatalytically evaluated by photodegradation of MB in the presence of a small amount of H_2O_2 under visible and UV light irradiation.

2. Experimental procedure

2.1. Materials and methods

All the reagents used in this study were purchased from Merck Company with analytical grade and used as received without any further purification. Copper nitrate ($Cu(NO_3)_3{\cdot}3H_2O$), copper acetate ($Cu(Ac)_2{\cdot}H_2O$), and copper sulfate ($(CuSO_4){\cdot}5H_2O$) were applied as precursors of copper oxide. The urea ($CO(NH_2)_2$) and CTAB were employed as a hydrolysis agent and a cationic surfactant, respectively [9]. The saturated Cu^{2+} solution was prepared by dissolving 0.26 M of each copper salt in 30 ml distilled water, separately. Then, 12 mmol of urea and 5.4 mmol of CTAB were added to each of the solutions under constant stirring for 15 min to form a blue homogeneous solution. Subsequently, the mixtures were transferred into a Teflon-lined stainless steel autoclave with 50 ml capacity and maintained at 180˚C for 6 h. Finally, the system was allowed to cool down to the room temperature. The resulting black precipitate was collected and washed with ethanol and distilled water for several times to remove anions and other impurities. Then, the samples were dried in a vacuum oven at 80˚C for 5 h. After this, the CuO powders which were produced by copper nitrate, copper sulfate, and copper acetate are denoted as CuO-Ni, CuO-Su, and CuO-Ac, respectively.

2.2. Characterizations

The crystalline structure of the prepared CuO samples was analyzed using an X-ray diffraction method (INEL EQUNOX 3000 diffractometer) with monochromatized Cu-Kα radiation ($\lambda = 1.541874$ Å) in the range of 20–70˚ with step size of 0.031. The optical characteristics of the samples were evaluated using a UV–Visible diffuse reflectance spectroscopy (DRS) from 190 to 900 nm by a MPC-2200 spectrophotometer. The morphology of the nanostructures was depicted by a scanning electronic microscope (SEM, Tescan Vega II). The SEM samples had been coated by a gold thin film by a desktop sputtering system (Nanostructured coating Co., Iran). Fourier transform infrared (FT-IR) spectra were recorded on a Shimadzu-8400S spectrometer in the range of 400–4,000 cm^{-1} using KBr pellets. Room temperature photoluminescence spectra (PL) were taken on a PL-Perkin-Elmer LS55 equipped with a 450 W Xe lamp as an excitation source. The active surface area of the samples was measured by Brunauer–Emmett–Teller (BET) method using a Micromeritics Gemini 2375 apparatus.

2.3. Photocatalytic procedure

In a typical process, the catalytic reaction was carried out in a 100 ml photoreactor, which contains 50 ml of MB dye (20 mgl^{-1}) solution and 0.005 g of catalyst. Before irradiation, the solution was stirred in the dark (60 min) for obtaining an equilibrium point of initial physical adsorption of MB over the surface of CuO samples. Irradiation was carried out using a combinatory light source of visible light (400 W tungsten lamp) and UV light (400 W high pressure mercury lamp). All photocatalytic experiments were accomplished at the same conditions. The distance between the surface of the MB solution and the light sources was about 20 cm. For determination of MB decolorization at specified periods, the lamps were turned off and 3 ml of each sample was collected and separated from the photocatalyst by centrifugation. The photocatalytic performance was indirectly monitored by relating the optical absorbance to the MB degradation amount using a double beam UV–Visible spectrophotometer at a wavelength of 664 nm.

3. Results and discussion

The FT-IR spectra of CuO samples synthesized by different precursors (CuO-Ni, CuO-Ac, and CuO-Su) are shown in Fig. 1. The main absorption peaks located at 436, 521, and 585 cm^{-1} are due to the formation of pure CuO monoclinic phase [10,26,27]. Since

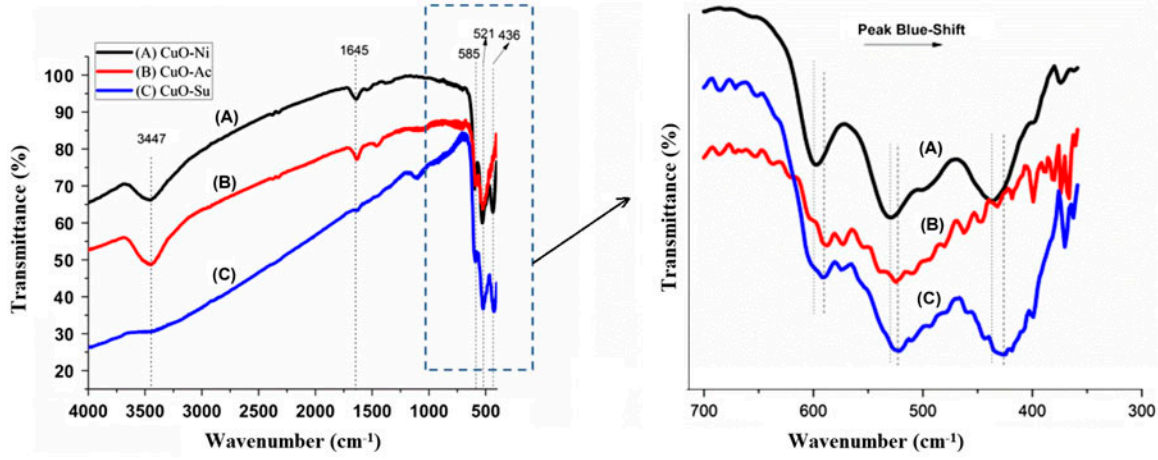

Fig. 1. The FT-IR spectra of the CuO samples fabricated by three different precursors: (A) CuO-Ni, (B) CuO-Ac, and (C) CuO-Su.

the anionic groups have considerable effects on the photocatalytic degradation reactions [28] for removing the unwanted effects of anions, the samples were post-washed many times by DI water and ethanol. As can be seen from FT-IR spectra, all of the samples have the same CuO-related peaks and no other functional groups are detected. On the other hands, the lack of any other peaks implies that unwanted impurities and phases are not present.

The peaks appeared at 3,455 and 1,645 cm^{-1} could be assigned to the stretching and bending vibrations of adsorbed water molecules and surface hydroxyl groups, respectively [27]. The observed blueshift of the low wavenumber peak is related to the size-induced variations in the lattice dimensions and the existence of crystal defects such as surface unsaturated coordination sites and edge dislocations [29]. It is also observed that the intensity of surface physical and/or chemical bonded H_2O and OH molecules CuO samples prepared from nitrate and acetate is much higher than that of CuO-Su sample. This observation could be related to the higher surface area of CuO-Ni and CuO-As samples.

The X-ray diffractions of the copper oxide nanostructures are shown in Fig. 2. All the observed peaks can be ascribed to the monoclinic CuO structure (JCPDS Card No. 05-0661). Moreover, two characteristic peaks at $2\theta = 35.6$ and 38.8° could be well indexed as $(\bar{1}\,1\,1)$–$(0\,0\,2)$ and $(1\,1\,1)$–$(2\,0\,0)$ planes of the CuO structure. Therefore, no other phases or impurities have been crystallized in the synthesis procedure.

The XRD results implied that the anion type of precursor salts can effectively adjust the crystallite size and lattice microstrain of as-crystallized CuO samples. According to the Williamson-Hall equation [30], peak

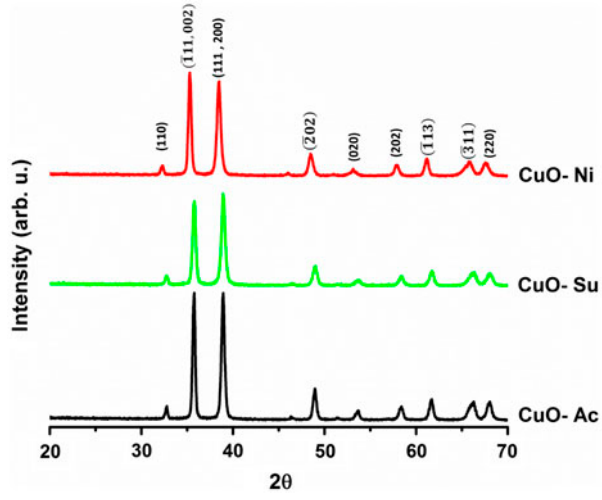

Fig. 2. The XRD patterns of hydrothermally grown CuO-Ni, CuO-Ac, and CuO-Su samples.

broadening is due to combination effects of apparent domain size (l) and lattice strain (η):

$$B_r.\cos\theta = \frac{K\lambda}{l} + \eta.\sin\theta \quad (1)$$

where λ is the X-ray wavelength (1.54 Å), K is the Scherrer constant (0.94), and θ is the Bragg angle. On the base of this equation, the width of diffraction peak, B_r, can be considered as the sum of widths due to crystallite sizes and mean lattice microstrains. The Williamson-Hall plots are presented in Fig. 3((A)–(C)). The slope of the fitted line is attributed to lattice microstrain. The positive slope of all fitted lines shows that tensile microstrain is induced in crystal lattice of

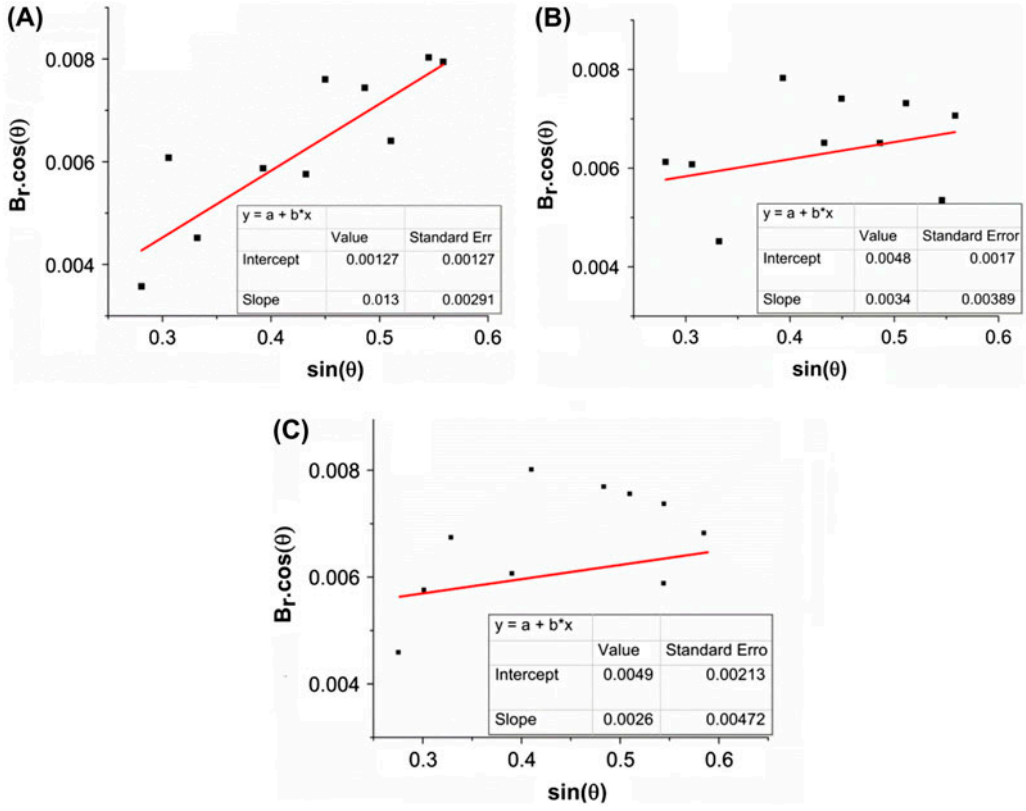

Fig. 3. Williamson-Hall plot of the different samples: (A) CuO-Ac, (B) CuO-Su, and (C) CuO-Ni.

all samples. The higher slope magnitude of CuO-Ac in comparison to that of CuO-Su and CuO-Ni suggests the enhancement of the lattice tensile strain where mean lattice microstrains (η) were calculated to be 0.0037, 0.0025, and 0.013% for CuO-Ni, CuO-Su, and CuO-Ac samples, respectively. The induced lattice strain is commonly originated from defects and lattice distortions in the crystals [31]. Moreover, the average crystallite sizes of the CuO were determined using the intersect value of the regression lines with the y axis. Concerning this, the average crystallite sizes were found to be 58, 123, and 44 nm for the CuO-Ni, CuO-Ac, and CuO-Su, respectively. The small value for CuO-Su is due to the effects of sulfate anions which suppress the preferential crystal growth in hydrothermal condition as it was observed by Abbasi and coworkers [32] in the case of ZnO.

The SEM images of CuO nanostructures are presented in Fig. 4. Different CuO morphologies obtained from various precursors might be related to the effects of anions on the growth of CuO nanostructures. It is suggested from Fig. 4(A) that nitrate anions facilitate the fast growth rate of the CuO nanostructure in a preferential orientation as a nanorod shape, which is in good agreement with the results of ZnO hydrothermal growth [31]. Fig. 4(B) shows an aggregated nano- and micro-powder synthesized from copper acetate precursor. It has been suggested that acetate anions could adsorb over the preferential planes and ban the growth of CuO in the specific orientations resulting in shapeless nanopowder growth [33]. Fig. 4(C) shows the nanoflake candle-like morphology (the thickness of layers are about 30 nm and average diameter of candles are about 1.4 μm). As can be seen, sulfate anions suppress the preferential growth of CuO crystals and nanoflake features are formed. It has been confirmed that sulfate anions may block some active sites of the metal oxide surface [32]. Hence, the growth proceeds in more than one direction. Moreover, it can be observed that stabilized nanoflakes are bonded to each other to form a candle-like nanostructure.

Room temperature PL of CuO samples measured using an excitation wavelength of 390 nm is shown in Fig. 5. It can be seen that all samples exhibit strong peaks at ~1.87, 2.22, and 2.48 eV as well as a weak peak at ~1.50 eV. The PL peak located at ~1.50 eV is related to recombination of electron and holes at oxygen vacancies, whereas the other emission peaks are the band edge emissions from the new sublevels due to the structural defects of CuO lattice [34].

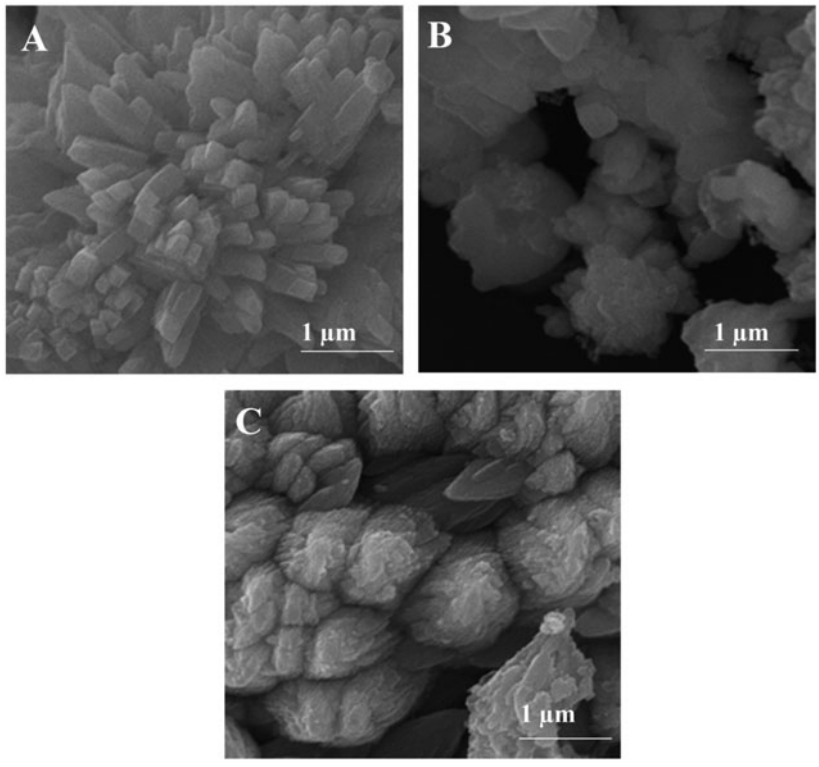

Fig. 4. The SEM images of the CuO samples fabricated by three different precursors: (A) CuO-Ni, (B) CuO-Ac, and (C) CuO-Su.

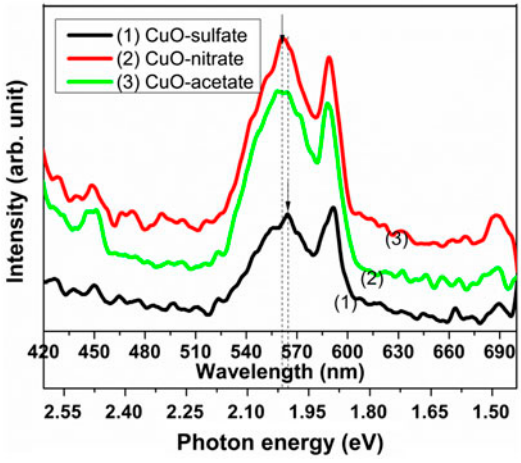

Fig. 5. The typical PL spectra of different structures grown in various precursors.

It is observed in the literature [35] that higher concentration of defects will result in higher green PL intensity. By comparing the spectra, it can be concluded that the much stronger and broader defect peaks of CuO-Ni and CuO-Ac are related to their higher deep level defects compared with that of CuO-Su sample. Moreover, the blueshift in the PL peak position from CuO-Su to CuO-Ac is attributed to the Burstein–Moss effect resulting from small sized particles, which is in good agreement with the SEM images.

Fig. 6 shows the N_2 adsorption and desorption of the CuO-Ni sample at 77 K. The results were analyzed using Belsorp data analysis software and showed that the BET surface area of samples were 64.8, 61.2, and 52.4 m^2g^{-1} for CuO-Ni, CuO-Ac, and CuO-Su, respectively. This result is in good agreement with the SEM images, where hierarchical structure of CuO nanorods seems to have the lowest tendency for aggregation.

The DRS measurements of the CuO samples are shown in Fig. 7(A). In addition, optical band gap of samples were calculated using the well-known Tauc method [36]. Generally, the Tauc relation is written as:

$$(\alpha h\nu)^{\mathrm{p}} = A(h\nu - E_{\mathrm{g}}) \tag{2}$$

where α is the absorption coefficient, E_{g} is the optical band gap, A is a constant related to the effective mass, $h\nu$ is the photo energy, and is the power depending upon the type of optical transition between the valence and conduction bands which takes the value

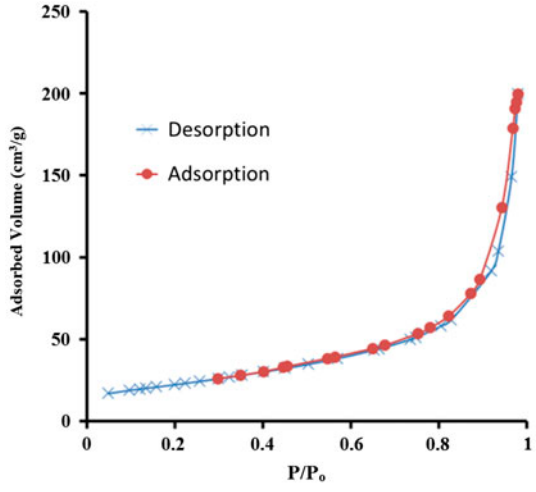

Fig. 6. The N_2 gas adsorption–desorption isotherm of CuO-Ni sample at 77 K.

two for direct transition and ½ for indirect transition [36]. The corresponding band gap energy, E_g, would be obtained by extrapolating a linear fitting from the $(\alpha h\nu)^p$ vs. $h\nu$ plot and interaction on the $h\nu$ axis. The calculated optical band gaps summarized in Fig. 7(B) implies that band gap values of all samples are almost identical and close to the band edge emission peak of the PL curves. These nearly same values could be explained by the fact that all samples were crystallized in a similar monoclinic crystal structure.

Copper oxide nanostructures have an important application in photodegradation of dye pollutants in the presence of H_2O_2. MB was chosen as a model pollutant to study photocatalytic reaction of CuO. Fig. 8(A) shows a comparison of the photocatalytic activity of CuO nanostructures prepared by three different precursors for degradation of MB under visible light radiation for 180 min in the presence of H_2O_2. The activity photocatalytic degradation of CuO-Ni is better than that of CuO-Su and CuO-Ac under visible light irradiation. Fig. 8(B) illustrates the photocatalytic degradation of MB in presence of only H_2O_2 as compared to that in presence of H_2O_2 and CuO-Ni under visible and UV light radiation. This figure reveals that H_2O_2 can alone destroy the MB structure, but the photodegradation amount of MB is higher in presence of CuO nanostructures and H_2O_2. On the other hands, MB degradation efficiency of CuO-Ni in the visible light is better than UV light irradiation (the degradation percentage of MB solution with concentration of 20 mgl^{-1} was about 100% at 180 min under visible light irradiation). The low band gap of CuO-Ni and increased activity of this semiconductor in visible light can thus be confirmed.

By monitoring the MB absorption peak at 665 nm, the plots of the percentage degree of degradation vs. reaction time were obtained for the CuO samples under UV and visible light irradiation. The percentage degree of MB degradation was calculated by the following equation:

$$\%\ \text{Degradation} = \frac{C_0 - C}{C_0} \times 100 \tag{3}$$

where C_0 and C are the initial and final concentrations of MB, respectively. The percentage degree of MB photodegradation (with different initial concentration of 5, 10, and 20 mgl^{-1}) vs. reaction time was investigated in presence of CuO-Ni and H_2O_2 under visible and UV light irradiation (Fig. 9((A)–(D))). The kinetics

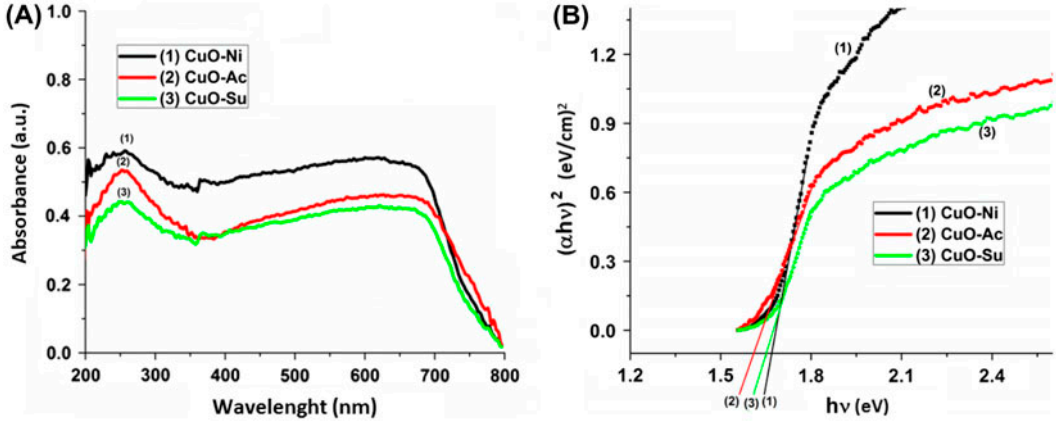

Fig. 7. (A) DRS and (B) the Tauc plot of $(\alpha h\nu)^2$ vs. $h\nu$ of the CuO samples fabricated by different precursors.

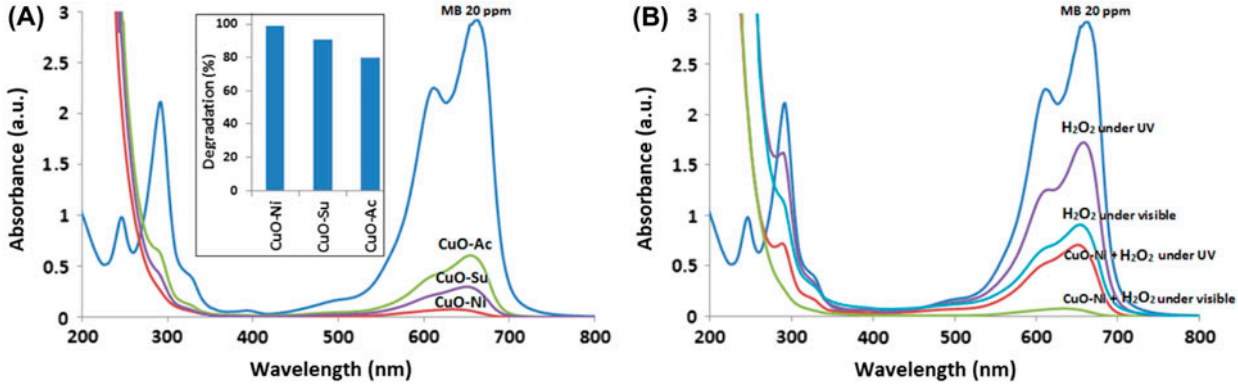

Fig. 8. (A) The photocatalytic degradation of MB in the presence of the CuO nanostructures and H_2O_2 under visible light radiation at 180 min and (B) the photocatalytic degradation of MB in presence of only H_2O_2 and as compared to H_2O_2 and the CuO nanostructures under visible and UV light radiation [conditions: 50 ml MB with initial concentration of 20 mgl^{-1}, 0.05 g photocatalyst, and 180 min reaction time].

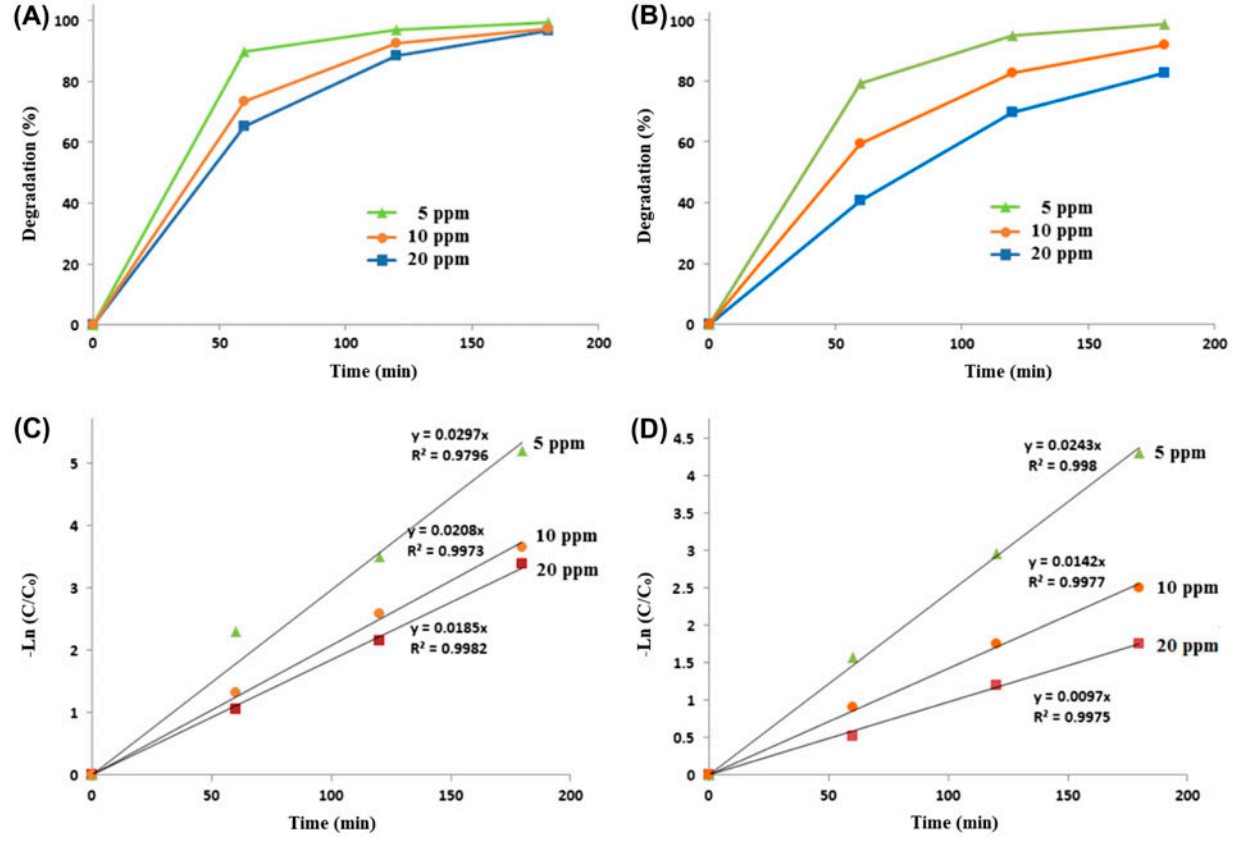

Fig. 9. The photodegradation of MB vs. time in the presence of CuO-Ni and H_2O_2 under (A) visible (B) UV light irradiation. The degradation rate constant modeled with a pseudo-first-order kinetic function under (C) visible, and (D) UV light irradiation [conditions: 50 ml MB with initial concentrations of 5, 10, and 20 mgl^{-1}, 0.05 g photocatalyst, and 180 min reaction time].

of these degradation reactions were investigated too. The photodegradation reaction of MB by CuO-Ni exhibited a pseudo-first-order kinetic model which is expressed as follows:

Table 1
The rate constant and R^2 (linear regression) of photodegradation reaction of MB by CuO-Ni catalyst under visible irradiation

Ln (C/C_0) (ppm)	k	R^2
Vis—5	0.029	0.979
Vis—10	0.02	0.997
Vis—20	0.018	0.998
UV—5	0.024	0.998
UV—10	0.014	0.997
UV—20	0.008	0.997

$$-\ln\frac{C}{C_0} = kt \quad (4)$$

where C_0 is the initial concentration of a pollutant, C is MB concentration at time t, and k is the rate constant of first-order reaction. The amount of k for different photodegradation reactions can be obtained by determining the slope of curves (Table 1).

It is clear that the initial concentration of MB effects on the rate of the photocatalytic degradation reaction. The increased concentration of MB leads to the reduction of the reaction rate, because the absorbance of light by the MB molecules increases. Therefore, fewer photons reach the active sites in CuO samples. On the other hands, the degradation reaction may be controlled by the limited active site number on the catalyst surface, whereas the same amount of CuO was used at the different initial concentrations.

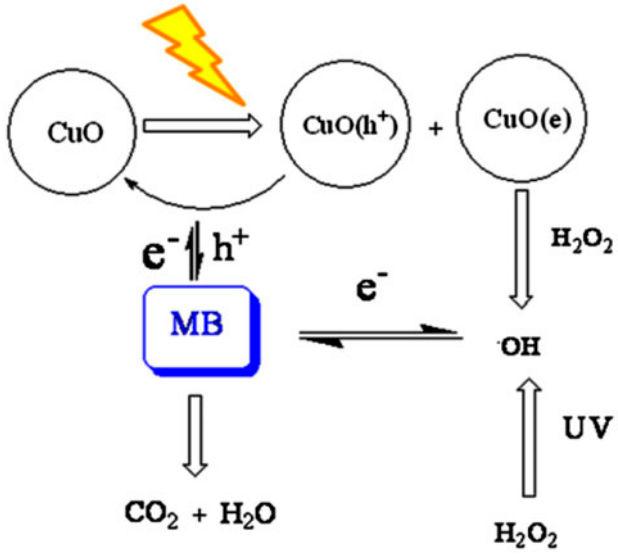

Fig. 10. Degradation of MB in the presence of CuO and H_2O_2 under light irradiation.

In many researches, H_2O_2 has been employed as a green additive to enhance the photocatalytic efficiency of CuO. It mainly acts as the electron acceptor and can be converted to $OH^{\cdot}$ radical after obtaining the electron under light radiation (Fig. 10). The electrons and holes are generated on the copper oxide surface under light radiation. The H_2O_2, as an electron acceptor, decrease the electron–hole recombination rate by accepting the electrons from the surface of CuO to produce $OH^{\cdot}$. Therefore, the stability of holes increases in the photocatalytic oxidation of MB. The H_2O_2 is converted to $OH^{\cdot}$ radicals under direct decomposition of H_2O_2 by light which directly oxidize MB at the same time.

4. Conclusions

In summary, various morphologies of CuO nanostructures were synthesized through a simple hydrothermal method. Study on the structures of the samples shows that the samples, independent of the precursor type, were crystallized in monoclinic crystal structure. The results of the N_2 adsorption–desorption and the photoluminescence of samples show that CuO nanorods grown with nitrate precursor have the highest active surface area. The FT-IR results showed that the concentration of surface OH^- group on the surfaces of the samples varies considerably according to CuO-Ac > CuO-Ni > CuO-Su. The nearly similar optical band gap of the samples could be attributed to the formation of the same phase in all synthesized samples. The photocatalytic performance of the samples was verified by MB decolorization under UV and visible light. According to the results, the CuO fabricated with copper nitrate showed the highest photocatalytic activity in the presence of H_2O_2 activator. The better photocatalytic performance of the CuO-Ni nanorods was assigned to its highest active surface area and considerable surface OH^- groups. Concerning that the H_2O_2 and CuO are readily available and have no harmful side effects on photocatalytic performance, the CuO-Ni nanorods can be introduced as a photocatalytic decomposer of organic pollutants using solar irradiation.

References

[1] F. Bayansal, B. Sahin, M. Yuksel, N. Biyikli, H.A. Cetinkara, H.S. Guder, Influence of coumarin as an additive on CuO nanostructures prepared by successive ionic layer adsorption and reaction (SILAR) method, J. Alloys Compd. 566 (2013) 78–82.
[2] A. Chowdhuri, V. Gupta, K. Sreenivas, R. Kumar, S. Mozumdar, P.K. Patanjali, Response speed of SnO_2-based H_2S gas sensors with CuO nanoparticles, Appl. Phys. Lett. 84 (2004) 1180–1182.

[3] A.E. Rakhshani, Preparation, characteristics and photovoltaic properties of cuprous oxide—A review, Solid-State Electron. 29 (1986) 7–17.
[4] J. Herion, E.A. Niekisch, G. Scharl, Investigation of metal oxide/cuprous oxide heterojunction solar cells, Sol. Energy Mater. 4 (1980) 101–112.
[5] C.L. Carnes, K.J. Klabunde, The catalytic methanol synthesis over nanoparticle metal oxide catalysts, J. Mol. Catal. A: Chem. 194 (2003) 227–236.
[6] X.P. Gao, J.L. Bao, G.L. Pan, H.Y. Zhu, P.X. Huang, F. Wu, D.Y. Song, Preparation and electrochemical performance of polycrystalline and single crystalline CuO nanorods as anode materials for Li ion battery, J. Phys. Chem. B 108 (2004) 5547–5551.
[7] W. Gao, S. Yang, S. Yang, L. Lv, Y. Du, Synthesis and magnetic properties of Mn doped CuO nanowires, Phys. Lett. A 375 (2010) 180–182.
[8] O. Eibl, Application of a new method for absorption correction in high-accuracy, quantitative EDX microanalysis in the TEM: Analysis of oxygen in CuO-based high-Tc superconductors, Ultramicroscopy 50 (1993) 189–201.
[9] S. Wang, H. Xu, L. Qian, X. Jia, J. Wang, Y. Liu, W. Tang, CTAB-assisted synthesis and photocatalytic property of CuO hollow microspheres, J. Solid State Chem. 182 (2009) 1088–1093.
[10] S. Xu, A.J. Du, J. Liu, J. Ng, D.D. Sun, Highly efficient CuO incorporated TiO_2 nanotube photocatalyst for hydrogen production from water, Int. J. Hydrogen Energy 36 (2011) 6560–6568.
[11] N. Mukherjee, B. Show, S.K. Maji, U. Madhu, S.K. Bhar, B.C. Mitra, G.G. Khan, A. Mondal, CuO nanowhiskers: Electrodeposition, Raman analysis, photoluminescence study and photocatalytic activity, Mater. Lett. 65 (2011) 3248–3250.
[12] J. Li, F. Sun, K. Gu, T. Wu, W. Zhai, W. Li, S. Huang, Preparation of spindly CuO micro-particles for photodegradation of dye pollutants under a halogen tungsten lamp, Appl. Catal. A 406 (2011) 51–58.
[13] Y. Li, J. Liang, Z. Tao, J. Chen, CuO particles and plates: Synthesis and gas-sensor application, Mater. Res. Bull. 43 (2008) 2380–2385.
[14] T. Premkumar, K.E. Geckeler, A green approach to fabricate CuO nanoparticles, J. Phys. Chem. Solids 67 (2006) 1451–1456.
[15] X. Wen, W. Zhang, S. Yang, Synthesis of $Cu(OH)_2$ and CuO nanoribbon arrays on a copper surface, Langmuir 19 (2003) 5898–5903.
[16] H. Hou, Y. Xie, Q. Li, Large-scale synthesis of single-crystalline quasi-aligned submicrometer CuO ribbons, Cryst. Growth Des. 5 (2004) 201–205.
[17] J. Liu, X. Huang, Y. Li, K.M. Sulieman, X. He, F. Sun, Hierarchical nanostructures of cupric oxide on a copper substrate: Controllable morphology and wettability, J. Mater. Chem. 16 (2006) 4427–4434.
[18] Y. Liu, L. Liao, J. Li, C. Pan, From copper nanocrystalline to CuO nanoneedle array: Synthesis, growth mechanism, and properties, J. Phys. Chem. C 111 (2007) 5050–5056.
[19] Y. Zhang, S. Wang, X. Li, L. Chen, Y. Qian, Z. Zhang, CuO shuttle-like nanocrystals synthesized by oriented attachment, J. Cryst. Growth 291 (2006) 196–201.
[20] J. Zhu, H. Bi, Y. Wang, X. Wang, X. Yang, L. Lu, CuO nanocrystals with controllable shapes grown from solution without any surfactants, Mater. Chem. Phys. 109 (2008) 34–38.
[21] O. Akhavan, R. Azimirad, S. Safa, E. Hasani, CuO/Cu $(OH)_2$ hierarchical nanostructures as bactericidal photocatalysts, J. Mater. Chem. 21 (2011) 9634–9640.
[22] R. Azimirad, S. Safa, Photocatalytic and antifungal activity of flower-like copper oxide nanostructures, Synth. React. Inorg. Met.-Org., Nano-Metal Chem. 44 (2014) 798–803.
[23] H. Pang, F. Gao, Q. Lu, Morphology effect on antibacterial activity of cuprous oxide, Chem. Commun. (2009) 1076–1078.
[24] S. Zaman, A. Zainelabdin, G. Amin, O. Nur, M. Willander, Efficient catalytic effect of CuO nanostructures on the degradation of organic dyes, J. Phys. Chem. Solids 73 (2012) 1320–1325.
[25] L. Shi, C. Yang, X. Su, J. Wang, F. Xiao, J. Fan, C. Feng, H. Sun, Microwave-hydrothermal synthesis of CuO nanorods and their catalytic applications in sodium humate synthesis and RhB degradation, Ceram. Int. 40 (2014) 5103–5106.
[26] J. Xia, H. Li, Z. Luo, H. Shi, K. Wang, H. Shu, Y. Yan, Microwave-assisted synthesis of flower-like and leaf-like CuO nanostructures via room-temperature ionic liquids, J. Phys. Chem. Solids 70 (2009) 1461–1464.
[27] C. Suryanarayana, M.G. Norton, X-ray Diffraction: A Practical Approach, Plenum, New York NY, 1998.
[28] S. Ahmed, M.G. Rasul, W.N. Marten, R. Brown, M.A. Hashib, Heterogeneous photocatalytic degradation of phenols in wastewater: A review on current status and developments, Desalination 261 (2010) 3–18.
[29] C. Chen, Y. Zheng, Y. Zhan, X. Lin, Q. Zheng, K. Wei, Reduction of nanostructured CuO bundles: Correlation between microstructure and reduction properties, Cryst. Growth Des. 8 (2008) 3549–3554.
[30] M. Vaseem, A. Umar, Y. Hahn, D. Kim, K. Lee, J. Jang, J. Lee, Flower-shaped CuO nanostructures: Structural, photocatalytic and XANES studies, Catal. Commun. 10 (2008) 11–16.
[31] T. Vimalkumar, N. Poornima, C.S. Kartha, K. Vijayakumar, Effect of precursor medium on structural, electrical and optical properties of sprayed polycrystalline ZnO thin films, Mater. Sci. Eng. B 175 (2010) 29–35.
[32] M.A. Abbasi, Y. Khan, S. Hussain, O. Nur, M. Willander, Anions effect on the low temperature growth of ZnO nanostructures, Vacuum 86 (2012) 1998–2001.
[33] S. Cho, S.-H. Jung, K.-H. Lee, Morphology-controlled growth of ZnO nanostructures using microwave irradiation: From basic to complex structures, J. Phys. Chem. C 112 (2008) 12769–12776.
[34] Q. Zhang, K. Zhang, D. Xu, G. Yang, H. Huang, F. Nie, C. Liu, S. Yang, CuO nanostructures: Synthesis, characterization, growth mechanisms, fundamental properties, and applications, Prog. Mater. Sci. 60 (2014) 208–337.
[35] M. Guo, P. Diao, S. Cai, Hydrothermal growth of well-aligned ZnO nanorod arrays: Dependence of morphology and alignment ordering upon preparing conditions, J. Solid State Chem. 178 (2005) 1864–1873.
[36] G. Guerguerian, F. Elhordoy, C.J. Pereyra, R.E. Marotti, F. Martín, D. Leinen, J.R. Ramos-Barrado, E.A. Dalchiele, ZnO nanorod/CdS nanocrystal core/shell-type heterostructures for solar cell applications, Nanotechnology 22 (2011) 1–9, 505401.